

FULL PAPER

Open Access



Outer trench slope extension to frontal wedge compression in a subducting plate

Emmy T. Chang^{1*}  and Laetitia Mozziconacci²

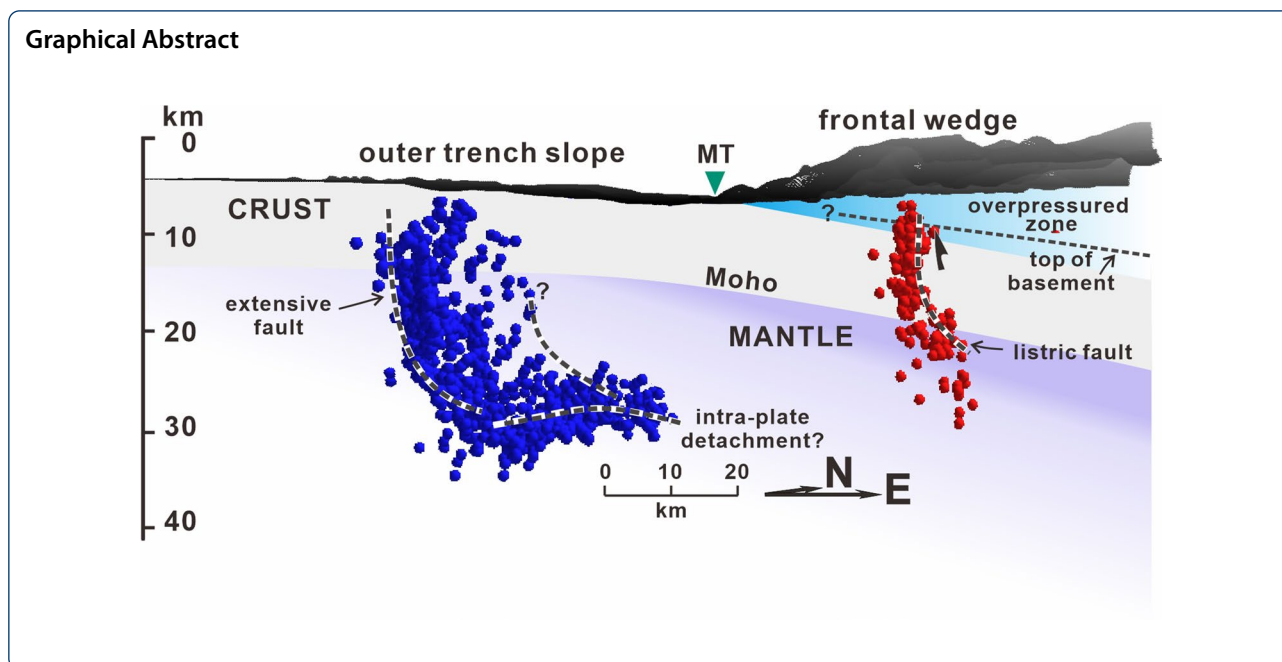
Abstract

The occurrence of faulting in subducting plates is a major process that changes the mechanical properties of the subducting lithosphere and carries surface materials into mantle wedges. Two ocean-bottom seismometer networks deployed on the frontal accretionary wedge of the northern Manila trench in 2005 and on the outer slope of the trench in 2006 were used to detect earthquakes in the subducting plate. All available P and S manually picked phases and the waveforms of 16 short-period, three-component stations were used. Relocation was performed using the double-difference method with differential times derived from the phase-picked data. Two intraplate earthquake sequences of small-to-moderate magnitudes in the northern Manila subduction system were investigated in this study. The results revealed distinct fault planes, but a contrasting seismogeny over the northern Manila Trench. The seismicity in the frontal wedge (as measured in 2005) was mainly contributed by a fluid overpressure sequence, whereas that in the incoming plate (as measured in 2006) was contributed by the aftershocks of an extensional faulting sequence. The obtained seismic velocity models and V_p/V_s ratios revealed that the overpressure was likely caused by high pore-fluid pressure within the shallow subduction zone. By using the near-field waveform inversion algorithm, we determined focal mechanism solutions for a few relatively large earthquakes. Through the use of data obtained from global seismic observations, we determined that stress transfer may be responsible for the seismic activity in the study area during the period of 2005–2006. In late 2005, the plate interface in the frontal wedge area was unlocked by the overpressure effect due to a thrusting-dominant sequence. This event changed the stress regime across the Manila Trench and triggered a normal fault extension at the outer trench slope in mid-2006. However, in the present study, a hybrid focal mechanism solution indicating reverse and strike-slip mechanisms was implemented, and it revealed that the plate interface locked again in late 2006.

Keywords: Ocean-bottom seismometer, Double-difference relocation, Seismic velocity model, Near-field focal mechanism solution, Northern Manila Trench, Fluid overpressure, Outer trench slope

*Correspondence: etychang@ntu.edu.tw

¹ Institute of Oceanography, National Taiwan University, Taipei 10617, Taiwan
Full list of author information is available at the end of the article



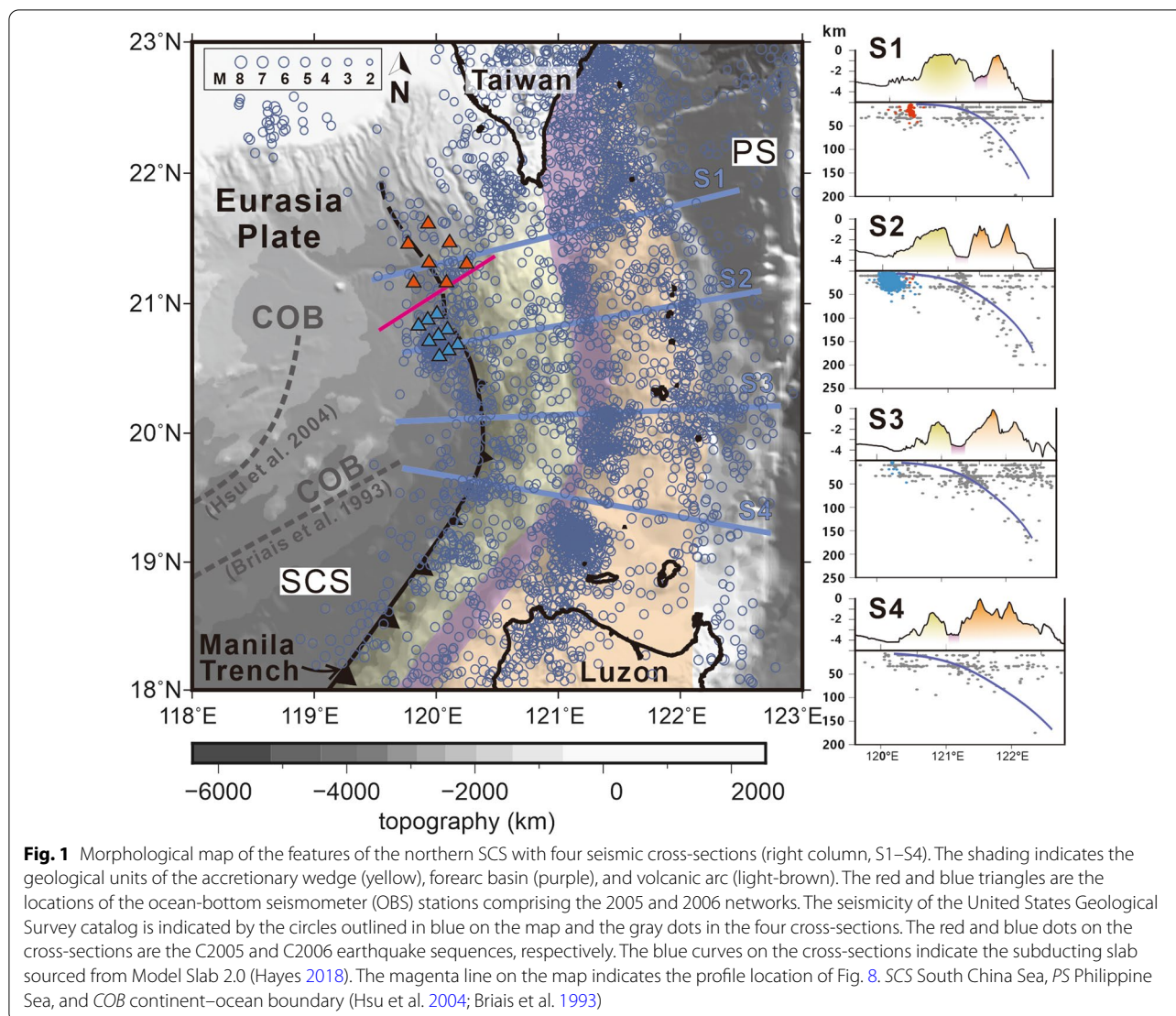
Introduction

Subducting slabs are considered the primary avenue through which fluid is transported into the Earth's mantle. Lithological fractures in the incoming plate and that are filled with unconsolidated water-rich sediments are considered potential fluid carriers; these fractures cause the mineral hydration of subduction systems (e.g., Peacock 1990; Audet et al. 2009; Audet and Schwartz 2013; Obana et al. 2012; Han et al. 2016; Faccenda et al. 2009; Faccenda 2014; Grevemeyer et al. 2018). Insertion of fluid into the lithosphere may trigger crustal eclogitization or mantle serpentinization, changing the mechanical structure of these regions during subduction (Schlaphorst et al. 2016). The mechanical properties of lithospheric fractures in subduction zones—which are affected by the lithospheric thickness, chemical composition, and the tectonic evolution of the plate—are crucial for the consequent processes in the subducted slab and mantle wedge.

In this study, we conducted a near-field seismic observation in the northern Manila subduction system to investigate faulting around the trench. In the study area, the South China Sea (SCS) seafloor is actively subducting beneath the Philippine Sea (PS) plate (Fig. 1). The Manila subduction system is situated between Taiwan and Luzon, and the plate convergent rate is approximately 100 mm/year near North Luzon, but is reduced to 50 + mm/year near Taiwan due to the collision of the PS plate against the Eurasian plate (Yu et al. 1999; Galgana et al. 2007). The magnetic anomaly in the central basin of the SCS indicates that seafloor spreading took place during the Oligocene to early Miocene (32–10 Ma) periods

in a north–south symmetric expansion (e.g., Taylor and Hayes 1983; Briais et al. 1993). Seismic profiles in the northern SCS reveal the relicts of the initial continental rifting, and continental crust thinning in the northern SCS can be further inferred (e.g., Wang et al. 2006; Cullen et al. 2010; McIntosh et al. 2013, 2014; Eakin et al. 2014). The continent–ocean boundary in the northern SCS has not yet been identified. On the basis of the time scales of the magnetic anomaly, the northeast SCS between the Eurasian continental margin and the Manila Trench has been determined to have the oldest crust in the SCS (i.e., 37 Ma from Hsu et al. 2004 and 32 Ma from Briais et al. 1993). Analyses of lithospheric mechanical strength by conducting flexural modeling have revealed significant variation in mechanical behavior for the subducting lithosphere (Zhang et al. 2018a, b; Li et al. 2019). The continent–ocean transition and weakening of the plate by flexural bending cause variation in lithospheric strength around the Manila Trench. Thus, the joint mechanism of basin spreading and plate subduction in the northeast SCS may generate local structures that indicate varied tectonic processes at different temporal and spatial scales.

We analyzed two earthquake groups occurring on opposite sides of the northern Manila Trench. Seismic data were acquired from seafloor networks of ocean-bottom seismometers (OBSs) independently deployed in 2005 and 2006. These networks are denoted Network 2005 and Network 2006, respectively. Network 2006 was located on the outer trench slope of the incoming SCS plate west of the Manila Trench (Fig. 1). Network



2005 was located northeast of the position of Network 2006, and it spanned the Manila Trench and the frontal area of the Taiwan accretionary prism (Fig. 1). Bathymetry for both networks indicated that their depths were approximately 4000 m on average.

Because of their limited battery capacity, the two OBS networks only recorded data for less than 1 week. Network 2005 was active from October 7 to 11, 2005, on the seafloor and comprised five short-period-response OBSs. Network 2006 was active from November 20 to 26, 2006, and had nine OBSs. Detailed station information is presented in Additional file 1: Table S1. Although the spatial aperture and duration of these experiments were limited, hundreds to thousands of earthquakes were recorded during the two experiments. The double-difference earthquake location method was used.

The accuracy of the relocated catalog is of the order of a few hundred meters. The resolved seismicity demonstrates the distinct fault geometries that extend through the crust and lithospheric mantle within the subducting SCS plate. The ratio of P- to S-wave velocity, V_p/V_s , is sensitive to lithological strength and water content (e.g., Domenico 1984; Christensen 1996). The high V_p/V_s ratios retrieved from the earthquake groups detected by Network 2005 indicate high water content within the top layers in the frontal accretionary area. We further determined the focal mechanism solutions by using the near-field waveform inversion method (Delouis 2014) for a few of the larger events in these two sequences to investigate the stress regime. Our results provide a close look at the seismic properties of the upper portion of the lithosphere in the subduction zone. A sharp

change in the seismogeny over the Manila Trench was discovered, and a triggering of earthquakes due to fluid overpressure in the frontal accretionary prism was identified.

Seismicity in the northern Manila subduction zone from global networks

The tectonic units in subduction between Taiwan and Luzon are, from west to east, the Manila Trench, the frontal wedge of the accretionary prism, the forearc basins, and the Luzon Volcanic Arc (Fig. 1). Approximately 3400 events are archived in the USGS global earthquake catalog (USGS: the United States Geological Survey, <https://earthquake.usgs.gov/earthquakes/search/>) for this area. Most are moderate earthquakes with magnitudes ranging from 3.0 to 5.0. The Wadati–Benioff zone corresponding to eastward subduction of the SCS can be identified to a depth of 200 km in northern Luzon, where it becomes shallower and less active as it approaches the Taiwan orogen (seismicity Profiles S1, S2, and S3 in Fig. 1). Apart from that in the Wadati–Benioff zone, most of the seismic activity between Taiwan and Luzon is in a few earthquake clusters distributed beneath the volcanic arc and in the forearc basin. These seismic clusters correspond to significant lateral shortening due to thrusting and strike–slip mechanisms.

Global earthquake catalogs indicate that the seismic activity over the northern Manila Trench is minor (Figs. 1 and 2 and Additional file 1: Figure S1). This may be the reason for the insufficient seismometer coverage for global seismic observation prior to 2000 and for the limited capacity of inland stations for offshore detection. A review of the USGS seismic catalog within the area in which Networks 2005 and 2006 were deployed was performed, and it indicated that only one of the sequences that occurred at the outer trench slope during the period from the middle to the end of 2006 was observable (the temporal evolution of the seismicity of the USGS catalog is detailed in Additional file 1: Figure S1). Figure 2 illustrates the focal mechanism solutions that were provided by the global CMT (GCMT <https://www.globalcmt.org/>; Dziewonski et al., 1981; Ekström et al., 2012) and Taiwan's regional broadband seismic network (<https://tecws1.earth.sinica.edu.tw/AutoBATS/>, hereafter termed as AutoBATS) for the period from July 2005 to December 2006. The GCMT mechanism solutions indicated that the 2006 sequence was caused by normal fault deformations involving fault planes that were parallel to the trench axis. This is consistent with other normal fault observations at the outer trench slope because the upper layer of the oceanic crust is under extensional stress caused by downward bending of the subducting lithosphere (e.g., Jones et al. 1978; Hilde 1983). The USGS

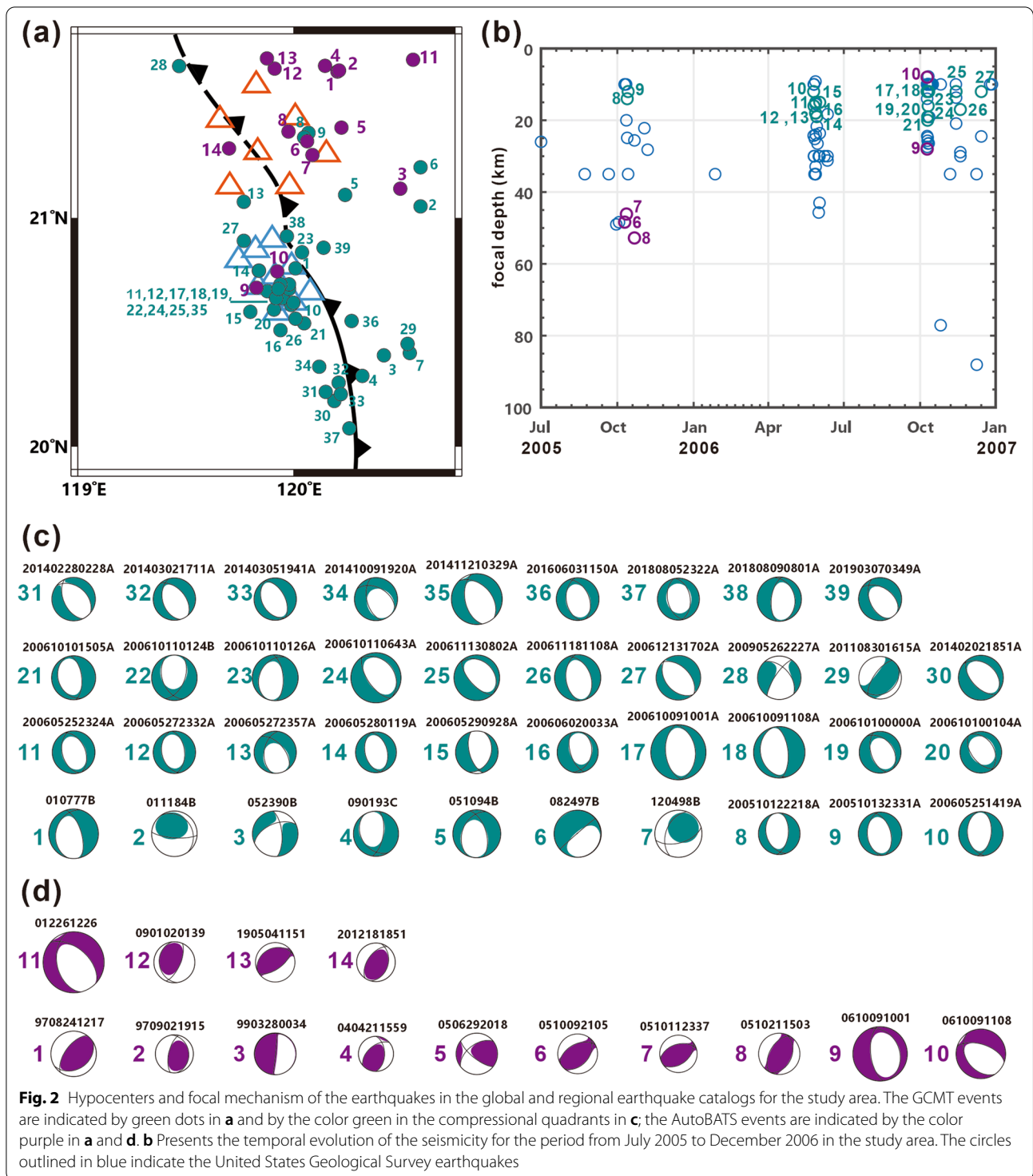
catalog indicated that this earthquake sequence began in May 2006. The earthquakes detected by Network 2006 in November 2006 were the aftershocks of this outer trench slope sequence.

However, within the coverage area of Network 2005, the GCMT results were not consistent with the AutoBATS results with respect to the mechanism of the sequence observed in 2005; the AutoBATS solution indicated a deformation in thrusting characterized by a strike–slip motion. In Fig. 2, Event 6 of the AutoBATS results was the mainshock of the sequence that started on October 9, 2005. Events 7 and 8 of the AutoBATS results were the two large aftershocks that occurred separately on October 11 and 21. These three AutoBATS solutions demonstrated a distinct thrusting mechanism in which the fault plane was in the NE–SW direction. However, Events 8 and 9 of the GCMT results revealed that another two aftershocks of the same sequence occurred on October 12 and 13, and a normal-faulting mechanism in which the fault plane was in the N–S direction was observed. In the results of our study and the data of the aforementioned two catalogs, all mainshocks and aftershocks occurred within a limited spatial regime. Therefore, the activation of the opposite seismic mechanism within a few days at a single specific site is a questionable phenomenon. Through the use of the data obtained from Network 2005, we generated results that were similar to those obtained through AutoBATS. The focal mechanism solutions of the 2005 sequence were a compound mechanism that comprised both thrusting and strike–slip deformations. In the following sections, we describe a distinct seismic pattern in the near-field OBS observations of the trench area.

Near-field OBS observations over the northern Manila Trench

The OBS instruments used in this study were short-period seismometers (MicrOBS) supplied by the L'Institut Français de Recherche pour l'Exploitation de la Mer. The MicrOBS data logger is stable and efficiently recorded ground motion in the frequency band of 1–100 Hz with a peak response at 4.5 Hz (Auffret et al. 2004). Seismic airgun shots preceded OBS deployments to relocate the seafloor OBS stations and to retrieve the recording directions of the two horizontal components (Chang et al. 2008). Prior to the outer trench slope sequence that occurred in 2006, we had already deployed Network 2005 at the lower slope of the frontal wedge in 2005 to detect the seismicity in the trench area.

We used the standard seismic program HYPOINVERSE-2000 (Klein 2002) to determine the earthquake hypocenters with direct P- and S-wave arrivals. To obtain a clean seismic onset for phase picking, we performed



basic preprocessing involving the removal of the mean from each seismic record and bandpass filtering of the data to remove long-period baseline drifting and high-frequency noise from the data. The frequency band of the bandpass filter was between approximately 0.1 and

30 Hz. For earthquake location, only the events that contained more than four clear seismic P- phases and one S-phase were located. This criterion was applied to screen out the numerous microseisms that were detected by fewer than four stations.

On the basis of the arrival times of seismic phases, we determined that the earthquake hypocenter was a trade-off for a velocity structure. The standard method is to iterate the process of accommodating a velocity structure and redetermining the location of an earthquake (Kissling et al. 1994). We adopted the model developed by Eakin et al. (2014; Profile T2, Fig. 11) for our initial P-wave velocity model (Fig. 3). The initial S-wave velocity was calculated by setting a V_p/V_s ratio of 1.74. On the basis of the hypocentral determination of the initial velocity model, we refined the P- and S-wave seismic velocities layer by layer from top to bottom by minimizing travel-time residuals and iteratively relocating the earthquakes. The program VELEST (Kissling et al. 1994) was employed to retrieve the optimized velocity model with each OBS experiment. After the earthquake locations and the velocity model were refined, events with a travel-time misfit of more than 0.3 s (approximately 5% of the events) were removed at this stage. Ultimately, the initial location that involved the routine process resulted in the identification of more than 400 and 2400 local earthquakes from the campaign records of Networks 2005 and 2006,

respectively. In accordance with the spatial range of focal depths, the retrieved seismic models defined the velocity structures approximately 25 and 35 km below the seafloor for Networks 2005 and 2006, respectively. Because unconsolidated sediments are distributed across the seafloor, we allowed for, but did not preset, a low-velocity layer in the topmost kilometers when developing the velocity models. Figure 3 presents the layered seismic models that were generated from the data of Networks 2005 and 2006; V_p/V_s was evaluated in terms of depth. These two seismic velocity models appear to be consistent with oceanic crust rather than continental crust. The velocity model obtained from the 2005 sequence indicated the presence of a dipping, downgoing oceanic crust structure with low-velocity sedimentary rocks on the top layers. In this study, zero focal depth indicates sea level.

To further improve location identification, we employed the hypoDD algorithm to obtain accurate relative hypocenter locations. The hypoDD method allows for the simultaneous relocation of a large number of earthquakes, which is achieved by determining the distances between correlated events that form the multiples

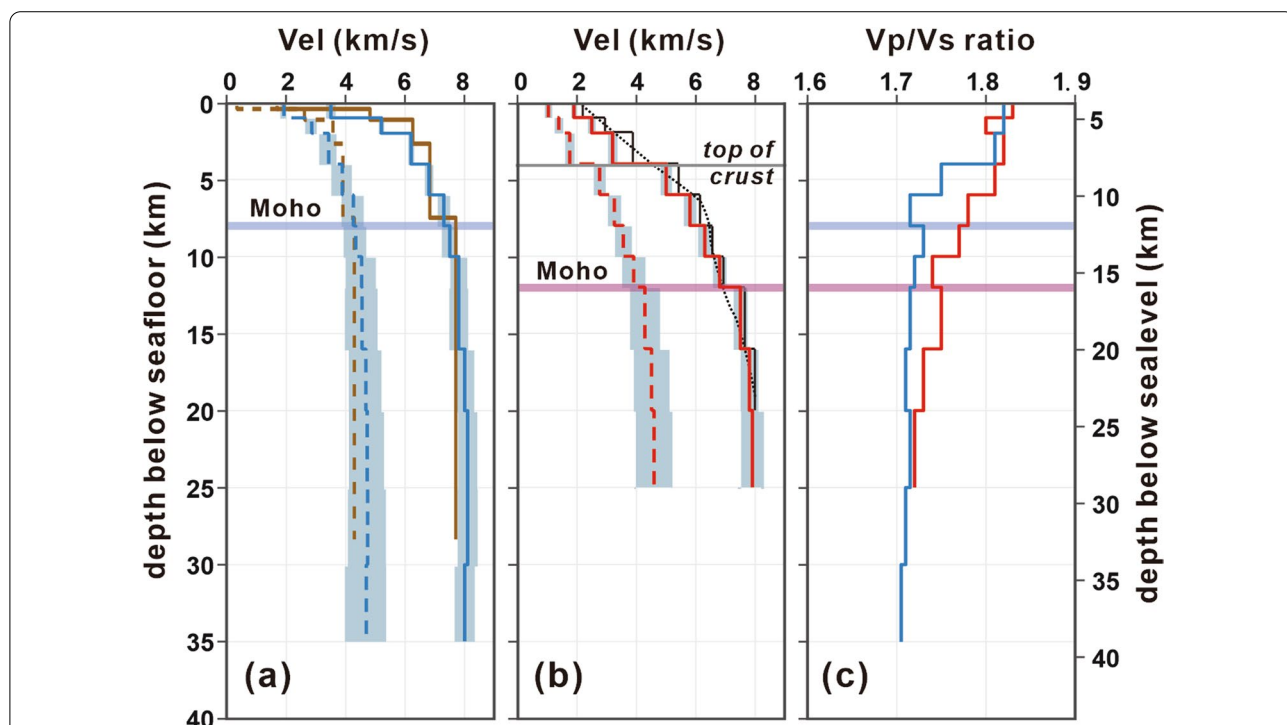


Fig. 3 Layered seismic wave (P- and S-waves) velocity models (a and b) and V_p/V_s ratio versus depth (c). The solid and dashed lines in the velocity models represent the P- and S-wave velocities, respectively. The red and blue lines in the V_p/V_s ratio plot represent the values from C2005 and C2006. Both the scales of depth from sea level and the seafloor are indicated. The gray-blue shadows along with the P- and S-wave velocity models indicate the uncertainties of the retrieved models. The velocity models for typical oceanic crusts are adopted from Laske et al. (2013); the models are indicated in a by brown lines. The initial velocity model (P-wave velocity) is adopted from Eakin et al. (2014); the model is indicated by the black line and black dashed line (modified by depth layers) in b

under the limit of the uncertainty (width) of the cross-correlation peak (Waldhauser 2001; Waldhauser and Ellsworth 2000). We obtained 388 and 1862 relocated events with the data of Networks 2005 and 2006, respectively.

Three statistical error estimates were applied to study location uncertainty, namely the root-mean-square (RMS) of travel-time residuals, the error in depth (ERZ), and the error in epicenter (ERH; Flinn 1965). The hypoDD relocation methods considerably reduced error estimates, and the RMS, ERZ, and ERH values following mitigation were less than 0.1 s and of the order of a few hundred meters. Figure 4 illustrates the location differences between the initial event location and the results of the hypoDD relocations. The relocated events exhibited a concentrated pattern in space, and some events in the initial location were located at very shallow depths, possibly due to the application of the layered velocity model at the location.

The aforementioned two relocated earthquake groups are referred to as C2005 and C2006 in the subsequent sections of the present study. The hypocentral parameters of C2005 and C2006 are listed in Additional file 1: Table S2. The temporal evolution of these groups is presented in Fig. 5. We analyzed magnitude–frequency relationships (i.e., the Gutenberg–Richter power law; Gutenberg and Richter 1944) to examine the magnitude of completeness of C2005 and C2006, which were determined to have a magnitude of completeness of approximately 1.0 and 1.5, respectively (Table 1, Fig. 5). The magnitude–frequency curves of these two sequences both exhibited high b -values (1.56 for C2005 and 3.28 for C2006), indicating a predominance of small earthquakes. Notably, both the M_c and b -value of C2006 were higher than those of C2005. Because the station coverage of Network 2006 is denser than that of Network 2005, this difference is likely not due to any differences in seismic detection capacity. Rather, the differences indicate a seismogenic discrepancy at the opposite sites of the trench.

The seismic parameters of these two groups of earthquakes are presented in detail as follows.

C2005: earthquakes in the frontal wedge of the overriding plate

C2005 comprised earthquakes occurring over a period of 5 days (October 7–11). A mainshock of magnitude 4.5 occurred on October 9 (Event 61 in Additional file 1: Table S2) and was recorded by Network 2005 at a depth of approximately 10 km. Before this event, microseisms were scattered within the shallow layers at approximately 5 km (Fig. 5). The seismicity increased

simultaneously with the emergence of the mainshock, and the focal depth distribution of C2005 was dramatically extended to approximately 25 km from sea level (Fig. 5). The accurate hypocentral determination reveals that this sequence was distributed in a spatially vertical zone over a depth range of 20 km. This type of spatial pattern is not commonly detected in the subduction zone. In the frontal wedge area, seismicity usually indicates a regime of hydrologic and tectonic processes with active faults. However, the seismogenic zone was identified on the basis of the presence of a décollement dividing an upper brittle-fracture-dominated domain overlying a lower ductile domain. Pore-water geochemical evidence reveals that along-fault flow occurs specifically in the upper brittle domain but is hydrologically isolated from fluids in the underlying footwall sediments (e.g., Cello and Nurr 1988; Tobin et al. 2001; Lin et al. 2009). The C2005 data indicated vital seismic activity in which an upthrust faulting emerged at the top crust of the frontal wedge area.

The seismic velocity model constructed with C2005 indicated low velocity for the top layers within 4 km from the seafloor. The P- and S-wave velocities were approximately <3.0 and <1.8 km/s, respectively, and the corresponding V_p/V_s ratio was >1.80. In particular, in the topmost layer (~1 km) the P- and S-wave velocities are as low as 1.9 and 0.6 km/s, respectively. V_p/V_s for this layer is 1.83. This low-velocity impedance is common in unconsolidated sediments at shallow accretionary prisms. Network 2005 was located in a field of widely distributed gas hydrate in southwest offshore Taiwan (e.g., Liu et al. 2006; Berndt et al. 2019). Thus, a high V_p/V_s ratio at the topmost layer was expected. At the depth of 4 km beneath the seafloor, the recorded P- and S-wave velocities were considerably higher at approximately 5.8 and 3 km/s, respectively. This substantial change in seismic velocity corresponded to the interface between accretionary sediments and the hard basement. However, the V_p/V_s ratio remains as large as 1.80 at the upper and lower layers of the sediment–hard rock interface (Fig. 3). We considered high fluid content at the interface as well as in the accretionary sediments in the frontal area. Notably, this is the depth level at which where we observed microseisms before the mainshock of Event 61; it is also the focal depth of the larger earthquakes (including the mainshock) of this sequence. We inferred, therefore, that the upper layers, comprising the sedimentary prism and the top crust, have high fluid content, and overpressure of this fluid is responsible for the earthquake sequence beginning on October 9.

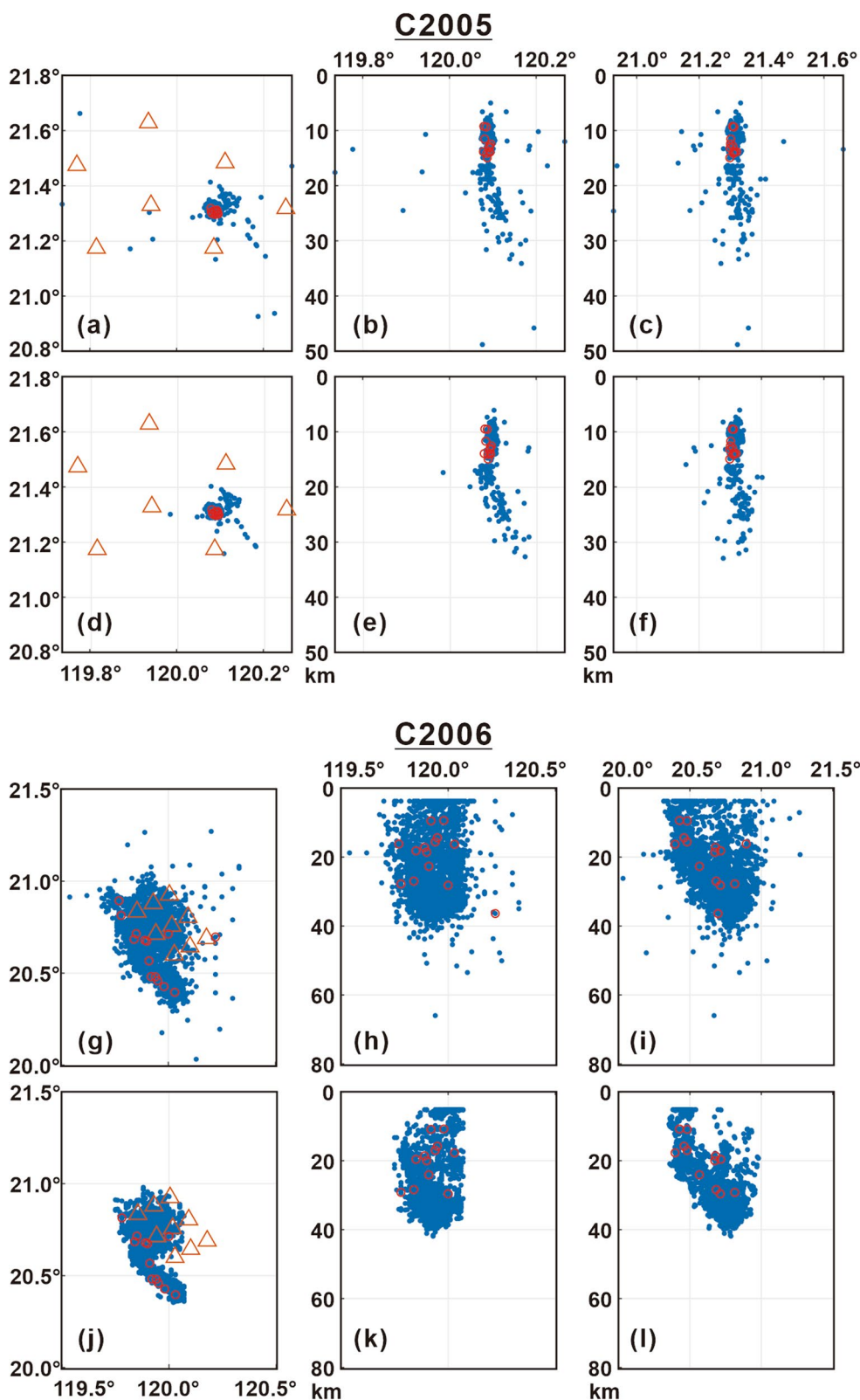


Fig. 4 Initial locations (a, b, c, g, h, i) and relocations (d, e, f, j, k, l) of the earthquake sequences detected in the present study. The circles outlined in red indicate the events of magnitude larger than 3.0. The OBS stations are presented in red triangles

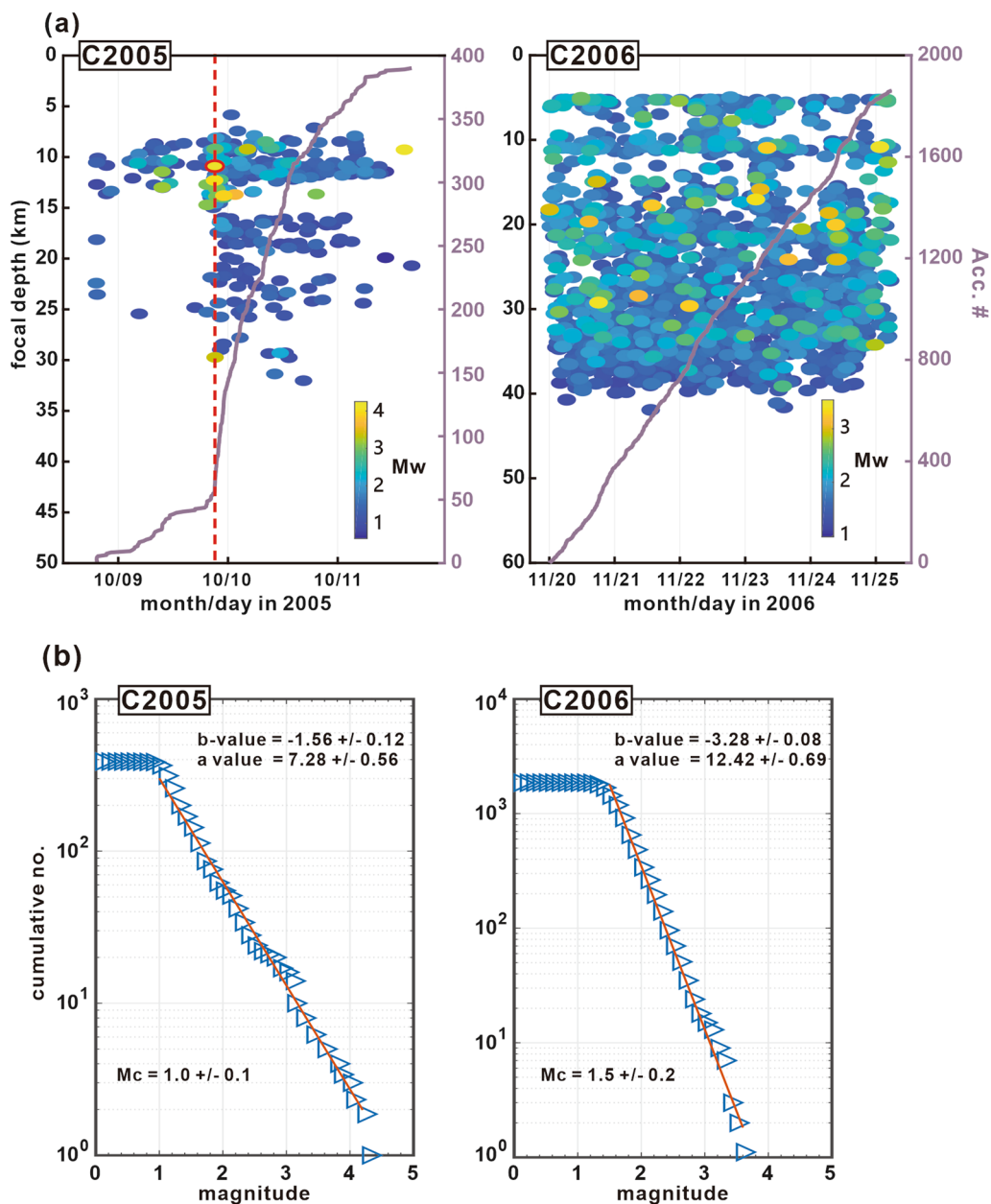


Fig. 5 **a** Temporal evolution of the seismicity detected in the present study; **b** the associated magnitude–frequency relationship curves. The main shock of C2005 is denoted by a red circle in **a**

Below 9 km, the seismic velocity increases and V_p/V_s decreases until approximately 16 km. At depths below 16 km, the seismic velocity is almost invariant; the P-wave velocity is approximately 7.8–8.0 km/s. However, V_p/V_s increases to 1.75 from 16 to 20 km. This may indicate a change in lithology from oceanic crust to lithospheric mantle. The Moho depth at the frontal wedge site should be approximately 16 km below the sea level, as revealed by the C2005 data.

C2006: earthquakes in outer trench slope of incoming plate

Network 2006 was located on the outer trench slope west of the Manila Trench, and earthquake magnitudes in C2006 ranged from 1 to 3.5 without temporal or spatial variation during the experimental period (Fig. 5). However, the seismicity rate in C2006 was as high as 400 events per day. Combining our result with the global seismic observations reveals that this bending–extensional

Table 1 The statistical error estimates of the averaged ERH, ERZ, and RMS from the initial location and the relocations in this study for the earthquake sequences detected by Networks 2005 and 2006

	RMS (second)	ERH (km)	ERZ (km)
Initial location of C2005	0.28±0.08	0.85±0.85	1.07±0.59
Relocation of C2005	0.12±0.04	0.08±0.06	0.15±0.12
Initial location of C2006	0.29±0.11	0.73±0.65	1.54±0.63
Relocation of C2006	0.15±0.06	0.27±0.11	0.19±0.14

sequence lasted for months—at least from the middle to the end of 2006.

The hypocenters of C2006 were categorized into two groups that formed two fault planes at different depth ranges, namely a high-angle north–south striking fault plane dipping to the northeast and extending from the seafloor to a depth of approximately 25 km and a flat fault plane at a depth of 20–35 km (Figs. 3 and 8). C2006 were the aftershock events of the extensional sequence initialized in the middle of 2006. Both GCMT and AutoBATS indicate a north–south striking normal fault for the large events of this sequence (Fig. 2). We recognize that the high-angle northeastward-dipping fault plane revealed by C2006 is the actual fault plane of this normal fault sequence. However, few clues regarding the formation mechanism for this low-angle fault with extensional deformation of the plate have been obtained. Based on the seismic velocities obtained in C2006, the Moho depth should be approximately 8 km below the seafloor (~12 km below sea level); at and below this depth, the P-wave velocity was as much as 7.6 km/s and invariant. This Moho depth reading is consistent with the previous active seismic surveys in this area (e.g., Wang et al. 2006; Eakin et al. 2014; Lester et al. 2014). That is, the flat-distributed seismicity in C2006 indicates deformation in the upper mantle.

Because the northeast SCS comprises relict structures from primitive basin spreading, we infer that the flat-distributed earthquakes of C2006 may be associated with a deep detachment fault, which is the lowest of the listric normal faults that are formed through hyperextension (Reston et al. 1996).

In addition to information about the Moho depth, the seismic velocity model from C2006 also indicates a relatively low lithological strength for the oceanic plate (Fig. 3). The P-wave velocity at the topmost layer was approximately 3.8 km/s, indicating the presence of solid materials at this level. However, the corresponding V_p/V_s ratio was greater than 1.80. This may indicate mechanical weakening or hydro fractures in the outer trench slope area caused by extensional fractures or indicate the filling

of the fractures by sediments with high fluid content, or both (e.g., Tobin et al. 2014).

Furthermore, the V_p/V_s ratios of C2006 were lower than those of C2005 at the layers above 20 km, indicating the occurrence of substantial dehydration when the plate was subducted into the mantle.

Focal mechanism solutions determined by near-field waveform inversion

We used the FMNEAR program to determine the focal mechanism solutions for the 29 larger earthquakes detected by our OBS networks. FMNEAR implements a near-field waveform inversion scheme to obtain focal mechanism solutions when there are few seismic stations. The detailed FMNEAR algorithm was described by Delouis (2014; <http://source.unice.fr:8080/FMNEAR/>). In practice, seven focal parameters—the strike, dip, rake, slip velocity (V_r), dislocation (Δu), and relative coordinates of the hypocenter and rupture center of the fault plane—are used in FMNEAR. Because the earthquakes detected in our experiment were all of small-to-moderate magnitude, the focal energy was assumed to have been emitted from a single point source. We also assumed that the rupture propagated circularly with constant velocity on the fault planes and assumed that the source time function was a simple ramp defined by a constant rise time (τ) and slip. Although the focal mechanisms of the small events were not substantially affected by the rise time, we adopted the empirical relationship proposed by Somerville et al. (1999), $\tau = \Delta u/V_r$, and used a simple V_r of 1 m/s. Combining the equation of seismic moment scaling (Hanks and Kanamori 1979) and the relationship of coseismic slip (Δu) with seismic moment, the slip Δu was determined as follows:

$$\Delta u = \frac{10^{\frac{3}{2}(M_W+10.7)}}{\mu L^2}, \quad (1)$$

where μ is the rigidity coefficient, equal to 3.5×10^{11} dyne/cm², and L^2 is the square of the rupture length. For all types of fault plane slipping, L^2 was obtained from the empirical relationship of the moment magnitude from Wells and Coppersmith (1994):

$$\log L^2 = -3.49 + 0.91M_W. \quad (2)$$

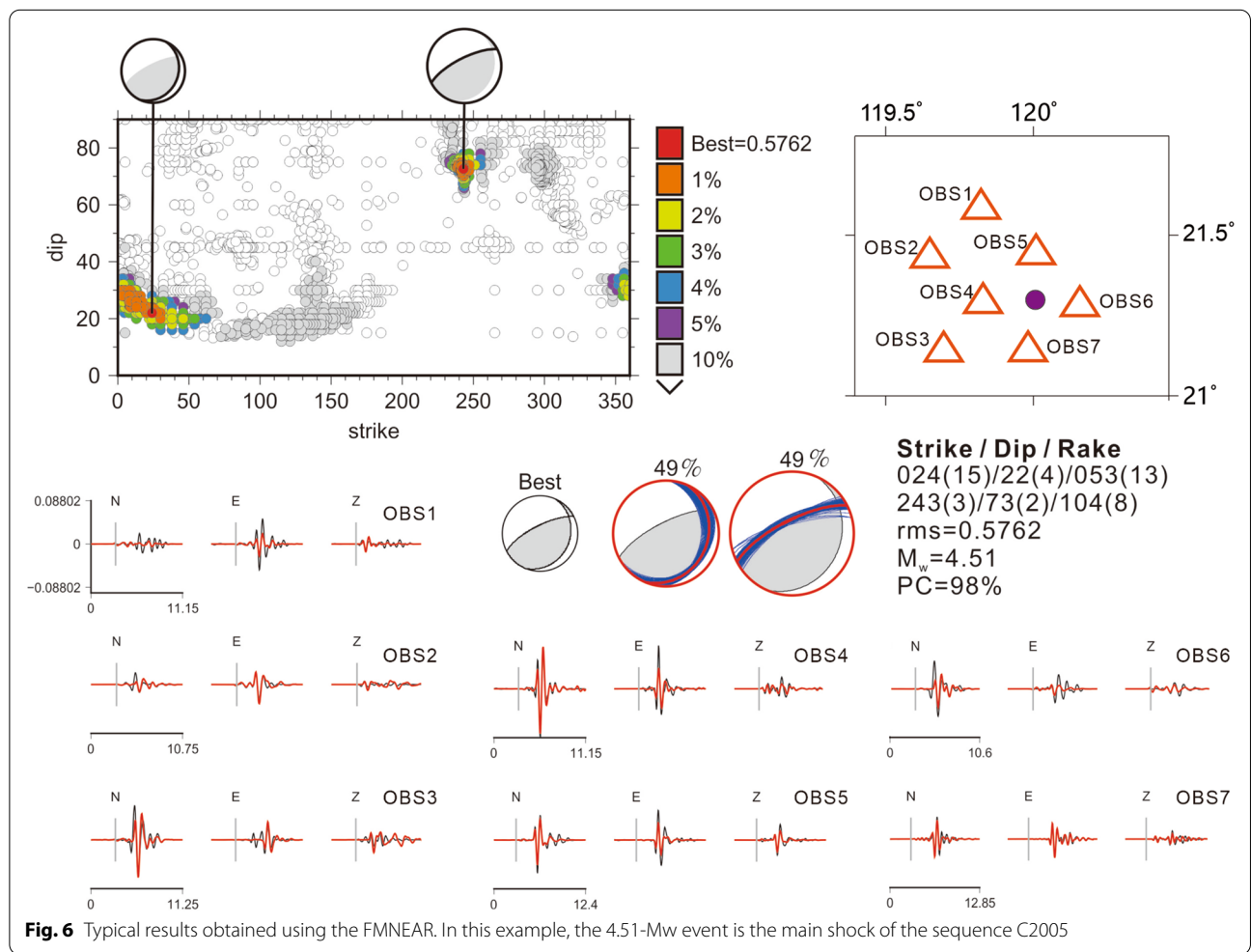
Therefore, the parameters Δu , L , and τ could be determined a priori for the inversion. The waveform segment covered a period of 3 s before the arrival of the P-wave to the end of the earthquake signal. The original waveform was integrated into the displacement and then treated using a bandpass filter of the remaining main motion signals. This process was then iteratively undertaken

for various fault parameters (i.e., strike, dip, and rake). The waveform fittings were conducted using the optimal seismic parameters obtained through the near-field waveform inversion. Because the code FMNEAR is specifically used for data processing to ensure the final quality of the inversion, the filtering of the waveforms is of paramount importance (e.g., Boore 2001). Delouis (2014) argued that, depending on the length of a signal window, an adapted high-pass filter (cutoff frequency of ~0.05 Hz) must be applied to avoid bias with respect to the reconstruction of the displacement signal. In practice, full waveforms are inverted. The data segment in the present analysis was between 10 and 15 s, approximately covering the time period from the 2 s before the arrival of the direct P-wave to the 5 s after the onset of the S-wave. In addition to high-pass filtering, a low-pass filter (cutoff frequency at ~5 Hz) had to be applied to remove the high frequencies that could not be properly modeled with a simple velocity model. Synthetic seismograms were subsequently calculated, and we considered the relocated hypocenter and magnitude as well as the refined 1D

velocity model that was adapted to the study area for the inversion.

Figure 6 presents the results pertaining to the main-shock of the 2005 sequence. This 4.51-Mw event was relocated at a depth of 11.06 km with a confidence of 98% through the use of a single point-source model and 21 channels of Network 2005. More examples of the FMNEAR analysis are presented in Additional file 1: Figure S3, which provides the statistics of the fitting residuals and the synthetic waveforms in inversion. The retrieved focal mechanism solutions are presented in Additional file 1: Table S3 and illustrated in Fig. 7.

In this study, the focal mechanism solutions determined from C2005 are those of relatively large events located at a depth of approximately 10 km. Those determined from C2006 are those of earthquakes vertically distributed at a depth range of 5–30 km; no solutions were identified from the flat seismicity group. The compressive (P) and tensional (T) axes are presented with their projections on the surface in Fig. 7. We further determined the stress regimes by using these focal



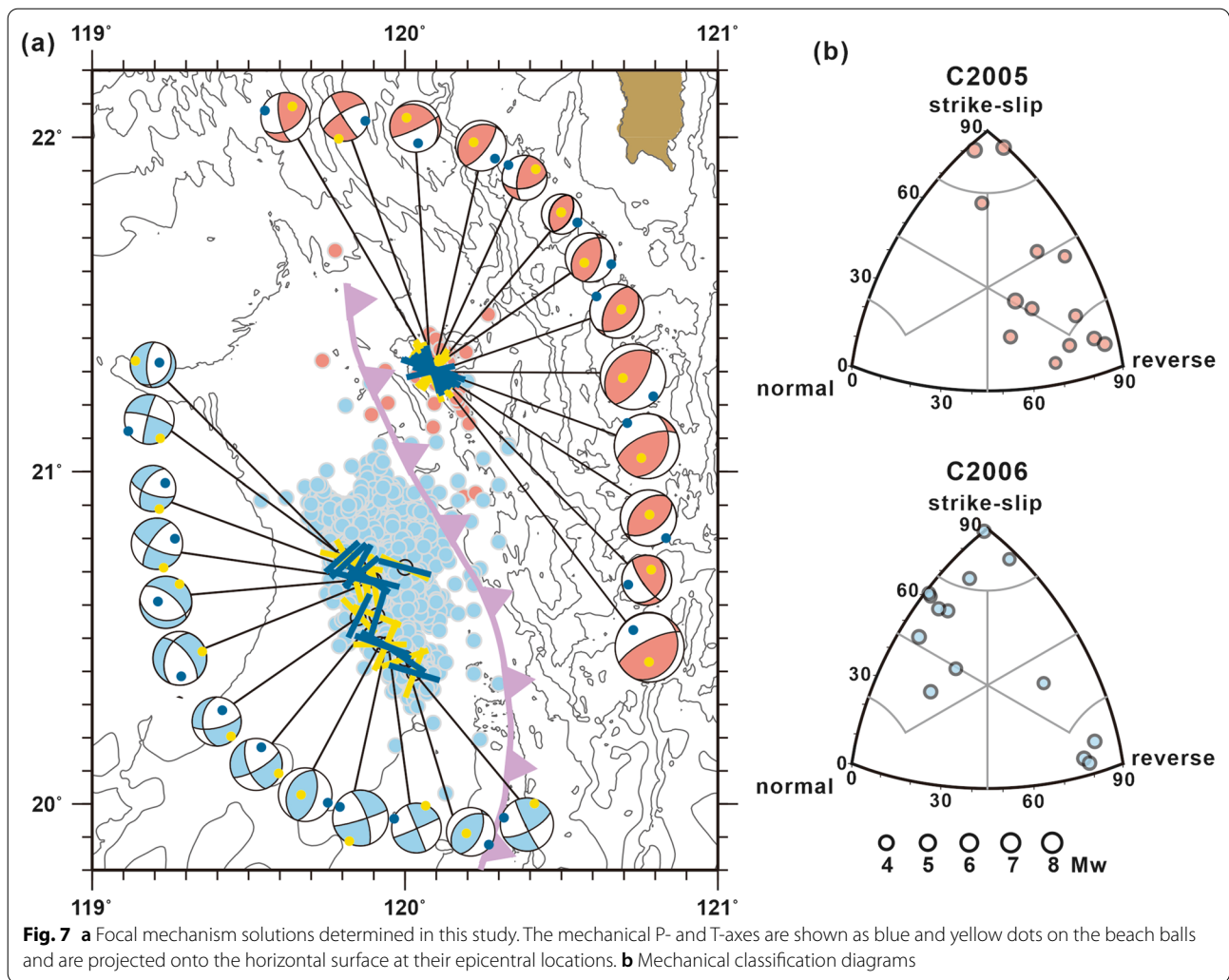


Fig. 7 **a** Focal mechanism solutions determined in this study. The mechanical P- and T-axes are shown as blue and yellow dots on the beach balls and are projected onto the horizontal surface at their epicentral locations. **b** Mechanical classification diagrams

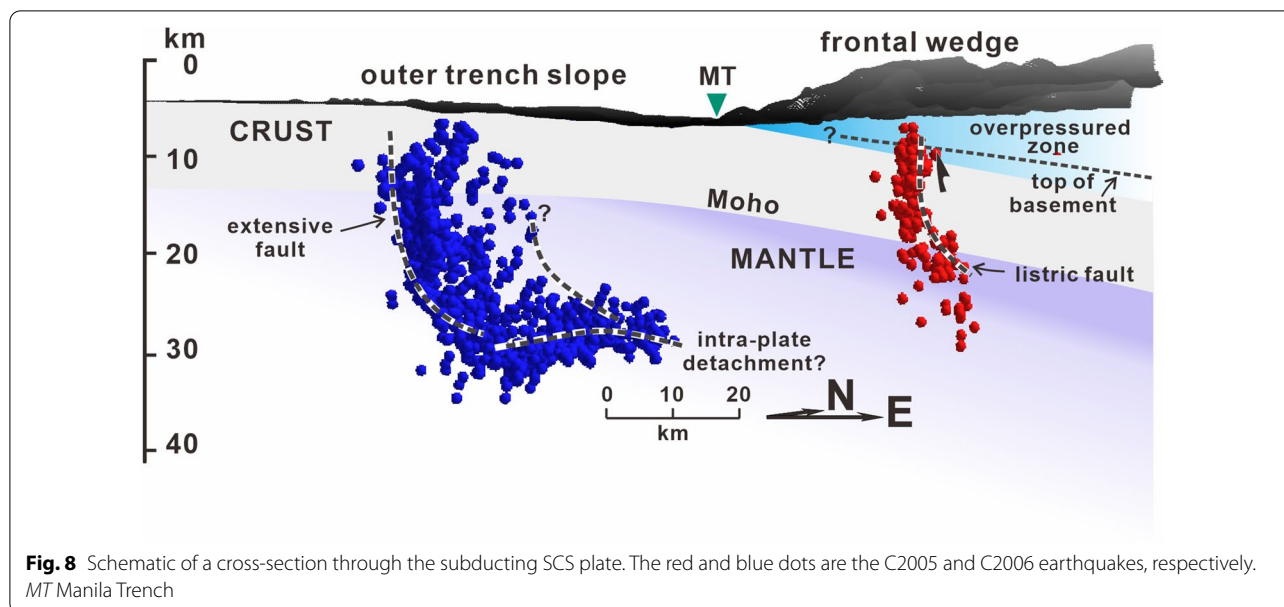
solutions. Álvarez-Gómez’s (2019) focal mechanism classification program was used to perform clustering analysis of the data and to generate a double-couple classification diagram through the Kaverina projection technique (Kaverina et al. 1996). The resulting mechanical classification is presented in Fig. 7.

Our results revealed that the seismic mechanisms of C2005 and C2006 included both thrusting failures and significant strike-slip deformations. As presented in Fig. 7, the P-axes derived from C2005 indicate an oblique-to-parallel orientation to the surface trace of the trench. Their principal direction follows the plate collision of the PS plate moving northwestward toward the Eurasian plate. However, these retrieved P-axes indicate a wide range of stress azimuths. This pattern may have been due to the uncertainty in our inversion.

However, analysis of C2006 indicates that the stress regime in the approaching plate is a strong strike-slip failure with the reverse mechanism. The distribution of the P- and T-axes of these solutions does not correspond to the extensional mechanism pattern of the outer trench slope area. In fact, the P- and T-axes retrieved from C2006 vary in space. Some solutions are even oriented oblique-to-perpendicular to the Manila Trench.

Discussion and conclusion

Our results reveal that the seismic activity level in marine convergent boundaries is far beyond the monitoring capacity of terrestrial seismic networks. By contrast with the high-magnitude tsunamigenic earthquakes occurring on subducting plate interfaces, the earthquakes detected in our study were intraplate earthquakes with



small-to-moderate magnitude. These events reveal the distinct seismotectonic properties of lithospheric deformation during subduction: the C2006 earthquakes were from a series of months-long aftershock events in the outer trench slope, whereas the C2005 earthquakes were primarily triggered by fluid overpressure in the frontal wedge area. Figure 8 presents the seismogenic patterns revealed in the above analyses as a schematic lithospheric cross-section of the subducting SCS plate (see the location indicated in Fig. 1). The spatial distribution of the C2006 events revealed that the high-angle fault plane at the outer trench slope developed through the crust and upper lithospheric mantle, whereas the flat-distributed seismicity formed a fault plane in the incoming plate in the lithospheric mantle. These two fault planes merge at a depth of approximately 30 km. In C2006, the V_p/V_s ratio indicates a weakening fracture in the topmost layer of the approaching plate. However, the hydrofracture effect did not appear to influence the lower crust or the upper mantle before the subduction of the plate into the mantle.

The crustal thickness was determined from the velocity model over approximately 8 km for the approaching plate as well as for the subducted slab. The velocity structure in the frontal area corresponded with a downgoing, dipping slab of the sedimentary prism with a low velocity in the upper 4 km. The relatively large V_p/V_s ratio through the crust level and the vertically penetrating seismicity reveal substantial effects caused by fluid in the slab beneath the frontal area. However, the classification of the focal mechanisms in the two groups (mostly from shallow events) revealed a significant thrusting component in both the C2005 and C2006 events. The contrast

in seismogeny of these two groups indicates possible temporal and fluid effects in this region; these are discussed separately in the following subsections.

Possible stress transfer within the northern Manila subduction system

The capacity of terrestrial stations to detect offshore seismic events is limited. Within the spatial frame of our two OBS networks, only one sequence (in 2006) was detected by the global seismic network in recent years. Combining the spatial and temporal seismogenic patterns from our result and the global catalog indicates that stress transfer may be responsible for the seismic activity in the study area in 2005–2006. In late 2005, overpressure in the frontal wedge unlocked the plate interface and triggered the thrusting-dominant sequence on October 9. This event changed the stress regime across the Manila Trench and triggered the normal fault extension at the outer trench slope in mid-2006. The hybrid focal solution for C2006 may have resulted from the plate interface having become locked again in late 2006, which restored the regional stress to laterally oblique convergence.

Notably, C2006 exhibited a change in the focal mechanism from the extension of the mainshock to the post-deformation lateral convergence. In fact, Obana et al. (2012) reported a similar observation for events on the outer slope of the Japan Trench. They discovered that the stress regime of the high-angle faults on the outer slope had temporal variation before and after the 2011 Tohoku earthquake. Variations in spatial and temporal stress range transferred between a subducted slab and approaching plate remain poorly understood in

subduction zone research; more observations of offshore earthquakes should be performed to better understand this topic.

Dehydration in the warm Manila subduction zone?

In a subduction zone, fluids are released from subduction-related prograde diagenetic-geochemical reactions at different depths. The fluids may escape from the uppermost sediments through lithological compaction and may form mud diapirism in the accretionary complex, which occurs in the strata 5 km beneath the seafloor, as indicated by seismic reflection images (e.g., Brown 1990; Henry et al. 1996). At the depth of the mantle wedge, fluids are released by metamorphic dehydration and react with mantle peridotites to form hydrous minerals (e.g., Syracuse et al. 2010; Keken et al. 2011). Recent studies have further identified the location of fluids exert in the subduction zones. Worzewski et al. (2010) obtained magnetotelluric images of the Costa Rican subduction zone and identified the accumulation of fluids at 20–30 km in the frontal accretionary area. In a similar study, Hu et al. (2017) revealed that epidote dehydration of mantle wedges at depths of 70–120 km led to anomalously high conductivities, particularly in the hot subduction zone. Condit et al. (2020) developed thermodynamic models with varied lithologies of the plate interface; these models predicted that major dehydration reactions could occur at shallower depths (25–65 km) in relatively warm subduction zones. Condit et al. further inferred that the shallow dehydration reaction may be responsible for nonvolcanic tremors and episodic slow-slip earthquakes. From these studies, it appears that the pathway through which fluids are released in subduction cannot be ascribed to a single set of circumstances.

The mechanical characteristics of earthquakes may serve as a proxy, indicating the presence of fluids in the accretionary prism and at the plate interface. Our study demonstrated that the C2005 events were mainly triggered by fluid overpressure at the top of the crust. The V_p/V_s ratios of C2005 were considerably higher than those of C2006 at both the crust and uppermost mantle levels, indicating high pore-fluid pressure when plate subducting underlying the accretionary prism. Because the sediment–crust interface is too shallow to match the temperature and pressure condition where dehydration reaction occurs, the fluids may transport from an up-dip migration of fluids from deeper in the mantle wedge. This would also indicate that the northern Manila subduction zone may be a warm subduction zone in which the fluids resulting from dehydration could be easily up to shallower layers.

Another potential mechanism for the high pore-fluid pressure in the deep frontal wedge is anisotropic permeability in the accretionary sediments. Pore-pressure profiles obtained from ocean drilling data (i.e., Saffer et al. 2000; Skarbek and Saffer 2009) indicate that strongly anisotropic permeability can cause basal sediments to remain undrained. Under this circumstance, a considerable volume of pore water may accumulate at the top of the oceanic crust. However, the seismicity of C2005 includes vertical faulting through the entire crust and down to the lithospheric mantle not only along with the plate interface; attributing the occurrence of C2005 solely to anomalous permeability at the basal sediments may not be accurate.

Based on the seismicity patterns and seismogenic characteristics conducted in this study, the fluids at the basal sediments might be sourced from thermodynamically constrained metamorphic reactions at shallow depths (according to Worzewski et al. 2010, depth of <30 km). This resulted in forming a fluid-oversaturated subduction channel at the base of the forearc crust, which was also demonstrated in the numerical modeling by Menant et al. (2019). Nevertheless, the anisotropic permeability can help to keep the basal sediments overpressured. We speculate that a warm subduction zone and anisotropic permeability of basal sediments may co-influence fluid distribution and seismogenic attribution in the northern Manila subduction zone.

Abbreviations

SCS: South China Sea; PS: Philippine Sea; OBS: Ocean-bottom seismometer; COB: Continent–ocean boundary; MT: Manila Trench.

Supplementary Information

The online version contains supplementary material available at <https://doi.org/10.1186/s40623-022-01664-9>.

Additional file 1: Table S1. Coordinates of the OBS stations. **Table S2.** Earthquake sequences C2005 and C2006. **Table S3.** Focal mechanism solutions retrieved in this study. The event numbers are from Table S2. **Figure S1.** The epicentral distribution of the events archived in the USGS and ISC-EHB catalogs. The event numbers of each catalog are shown at the title line. **Figure S2.** The temporal evolution of the seismicity illustrated by latitude (A1 and B1) and focal depth (A2 and B2) sections. (A1) and (A2): events inside the purple rectangular in Figure S1. (B1) and (B2) events in the period from July 2005 to December 2006. Two pink lines in A1 and A2 indicate the begin and end times for (B1) and (B2). **Figure S3.** Demonstration of the observed and synthetic waveforms in determining focal mechanism solutions.

Acknowledgements

We are grateful to the editor and two reviewers for their comments that helped us improve the manuscript. We would also like to extend our gratitude for the OBS instrumentation support provided by the Institute of Applied Geoscience, National Taiwan Ocean University, and for the support provided

by the Institute of Oceanography, National Taiwan University, with respect to the deployment of the crew of Ocean Research Vessel I. This study benefited substantially from the visit of the first author to JAMSTEC in 2019. The figures were prepared using the GMT software and with help from Haofang Hsueh and Fangyi Lee. This study was supported by the Ministry of Science and Technology, Taiwan, (Grant No. MOST 110-2611-M-002-012 –).

Author contributions

ETC: conceptualization, investigation, data curation, writing/original draft preparation, visualization, project administration. LM: methodology, software. Both the authors read and approved the final manuscript.

Funding

Ministry of Science and Technology, Taiwan, MOST 110-2611-M-002-012 –.

Availability of data and materials

The seismic parameters (hypocenter, focal mechanism solution) are provided in the Additional file.

Declarations

Competing interests

There are no competing interests to declare.

Author details

¹Institute of Oceanography, National Taiwan University, Taipei 10617, Taiwan.

²Institute of Applied Geosciences, National Taiwan Ocean University, Keelung 20224, Taiwan.

Received: 8 January 2022 Accepted: 14 June 2022

Published online: 29 June 2022

References

- Álvarez-Gómez JA (2019) FMC—Earthquake focal mechanisms data management, cluster and classification. *SoftwareX* 9:299–307
- Audet P, Schwartz SY (2013) Hydrologic control of forearc strength and seismicity in the Costa Rican subduction zone. *Nat Geosci* 6:852–855
- Audet P, Bostock MG, Christensen NI, Peacock SM (2009) Seismic evidence for overpressured subducted oceanic crust and megathrust fault sealing. *Nature* 457:76–78
- Auffret Y, Pelleau P, Klingelhofer F, Crozon J, Lin JY, Sibuet JC (2004) MicrOBS: a new ocean bottom seismometer generation. *First Break* 22:41–47
- Berndt C, Chi WC, Jegen M, Lebas E, Crutchley G, Muff S, Holz S, Sommer M, Lin S, Liu CS, Lin AT, Klaeschen D, Klauke I, Chen L, Hsu HH, Kunath P, Elger J, McIntosh KD, Feseker T (2019) Tectonic controls on gas hydrate distribution off SW Taiwan. *J Geophys Res Solid Earth* 124(2):1164–1184. <https://doi.org/10.1029/2018JB016213>
- Boore DM (2001) Effect of baseline corrections on displacement and response spectra for several recordings of the 1999 Chi-Chi, Taiwan, Earthquake. *Bull Seismol Soc Am* 91:1199–1211
- Briais A, Patriat P, Tapponnier P (1993) Updated interpretation of magnetic anomalies and seafloor spreading stages in the South China Sea: implications for the tertiary tectonics of Southeast Asia. *J Geophys Res Solid Earth* 98(B94):6299–6328
- Brown KM (1990) The nature and hydrogeologic significance of mud diapirs and diatremes for accretionary systems. *J Geophys Res Solid Earth*. <https://doi.org/10.1029/JB095iB06p08969>
- Cello G, Nurr A (1988) Emplacement of foreland thrust systems. *Tectonics* 7:261–272
- Chang E, Hsu SK, Lee CS (2008) Earthquake swarm recorded by an ocean bottom seismic array in southwest offshore of Taiwan in October, 2005. *Terr Atmos Ocean Sci*. [https://doi.org/10.3319/TAO.2008.19.6.717\(PT\)](https://doi.org/10.3319/TAO.2008.19.6.717(PT))
- Christensen NI (1996) Poisson's ratio and crustal seismology. *J Geophys Res Solid Earth* 101:3139–3156
- Condit CB, Guevara VE, Delph JR, French ME (2020) Slab dehydration in warm subduction zones at depths of episodic slip and tremor. *Earth Planet Sci Lett* 552:116601. <https://doi.org/10.1016/j.epsl.2020.116601>
- Cullen A, Reemst P, Henstra G, Gozzard S, Anandaroop R (2010) Rifting of the South China Sea: new perspective. *Pet Geosci* 16:273–282
- Delouis B (2014) FMNEAR: determination of focal mechanism and first estimate of rupture directivity using near source records and a linear distribution of point sources. *Bull Seismol Soc Am* 104(3):1479–1500. <https://doi.org/10.1785/0120130151>
- Domenico SN (1984) Rock lithology and porosity determination from shear and compressional wave velocity. *Geophysics* 49:1188–1195
- Dziewonski AM, Chou TA, Woodhouse JH (1981) Determination of earthquake source parameters from waveform data for studies of global and regional seismicity. *J Geophys Res* 86:2825–2852. <https://doi.org/10.1029/JB086iB04p02825>
- Eakin DH, McIntosh KD, Van Avendonk HJA, Lavier L, Lester R, Liu CS, Lee CS (2014) Crustal-scale seismic profiles across the Manila subduction zone: the transition from intraoceanic subduction to incipient collision. *J Geophys Res Solid Earth* 119(1):1–17. <https://doi.org/10.1002/2013jb010395>
- Ekdström GM, Nettles M, Dziewonski AM (2012) The global CMT project 2004–2010: Centroid-moment tensors for 13,017 earthquakes. *Phys Earth Planet Inter* 200–201:1–9. <https://doi.org/10.1016/j.pepi.2012.04.002>
- Faccenda M (2014) Water in the slab: a trilogy. *Tectonophysics* 614:1–30
- Faccenda M, Gerya TV, Burlini L (2009) Deep slab hydration induced by bending-related variations in tectonic pressure. *Nat Geosci* 2(11):790–793. <https://doi.org/10.1038/ngeo656>
- Flinn EA (1965) Confidence regions and error determinations for seismic event location. *Rev Geophys* 3:157–185
- Galgana G, Hamburger M, McCaffrey R, Corpus E, Chen Q (2007) Analysis of crustal deformation in Luzon, Philippines using geodetic observations and earthquake focal mechanisms. *Tectonophysics* 432(1–4):63–87
- Grevenmeyer I, Ranero CR, Ivandic M (2018) Structure of oceanic crust and serpentinization at subduction trenches. *Geosphere* 14(2):395–418
- Gutenberg B, Richter C (1944) Frequency of earthquake in California. *Bull Seismol Soc Am* 34(4):185–188
- Han S, Carbotte SM, Canales JP, Nedimovic MR, Carton H, Gibson JC, Horning GW (2016) Seismic reflection imaging of the Juan de Fuca plate from ridge to trench: New constraints on the distribution of faulting and evolution of the crust prior to subduction. *J Geophys Res Solid Earth* 121:1849–1872
- Hanks TC, Kanamori H (1979) A moment magnitude scale. *J Geophys Res* 84:2348–2350
- Hayes G (2018) Slab2—a comprehensive subduction zone geometry model. *US Geol Surv*. <https://doi.org/10.5066/F7PV6JNV>
- Henry P, Le Pichon X, Lallemand S, Lance S, Martin JB, Foucher JP (1996) Fluid flow in and around a mud volcano field seaward of the Barbados accretionary wedge: results from Manon cruise. *J Geophys Res* 101:20297–20323
- Hilde TW (1983) Sediment subduction versus accretion around the Pacific. *Tectonophysics* 99(2–4):381–397
- Hsu SK, Yeh YC, Doo WB, Tsai CH (2004) New bathymetry and magnetic lineations identifications in the northernmost South China Sea and their tectonic implications. *Mar Geophys Res* 25(1–2):29–44
- Hu H, Dai L, Li H, Hui K, Sun W (2017) Influence of dehydration on the electrical conductivity of epidote and implications for high-conductivity anomalies in subduction zones. *J Geophys Res Solid Earth* 122(4):2751–2762. <https://doi.org/10.1002/2016JB013767>
- Jones G, Hilde T, Sharman G, Agnew D (1978) Fault patterns in outer trench walls and their tectonic significance. *J Phys Earth* 26(Supplement):S85–S101
- Kaverina AN, Lander AV, Prozorov AG (1996) Global creepex distribution and its relation to earthquake-source geometry and tectonic origin. *Geophys J Int* 125(1):249–265
- Kissling E, Ellsworth WL, Eberhart-Phillips D, Kradolfer U (1994) Initial reference models in seismic tomography. *J Geophys Res* 99:19635–19646
- Klein FW (2002) User's guide to HYPOINVERSE-2000, a Fortran Program to solve for Earthquake locations and magnitudes. U.S. Geological Survey, United States, p 123
- Laske G, Masters G, Ma Z, Pasyanos M (2013) Update on CRUST10—a 1-degree global model of Earth's crust. *Geophys. Res. Abstracts*, 15, Abstract EGU2013-2658

- Lester R, Van Avendonk HJA, McIntosh K, Lavier L, Liu CS, Wang TK, Wu F (2014) Rifting and magmatism in the northeastern South China Sea from wide-angle tomography and seismic reflection imaging. *J Geophys Res Solid Earth* 119:2305–2323
- Li F, Sun Z, Pang X, Liao J, Yang H, Xie H, Zhuo H, Zhao Z (2019) Low-viscosity crustal layer controls the crustal architecture and thermal distribution at hyperextended margins: modeling insight and application to the Northern South China Sea margin. *Geochem Geophys Geosystems*. <https://doi.org/10.1029/2019GC008200>
- Lin AT, Yao B, Hsu SK, Liu CS, Huang CY (2009) Tectonic features of the incipient arc-continent collision zone of Taiwan: implications for seismicity. *Tectonophysics* 479(1):28–42. <https://doi.org/10.1016/j.tecto.2008.11.004>
- Liu CS, Schnürle P, Wang Y, Chung SH, Chen SC, Hsuan TH (2006) Distribution and characters of gas hydrate offshore of Southwestern Taiwan. *Terr Atmos Ocean Sci* 17(4):615–644
- McIntosh K, van Avendonk H, Lavier L, Lester WR, Eakin D, Wu F, Liu CS, Lee CS (2013) Inversion of a hyper-extended rifted margin in the southern Central Range of Taiwan. *Geology* 41(8):871–874. <https://doi.org/10.1130/g34402.1>
- McIntosh K, Lavier L, Van Avendonk H, Lester R, Eakin D, Liu CS (2014) Crustal structure and inferred rifting processes in the northeast South China Sea. *Mar Pet Geol* 58:612–626. <https://doi.org/10.1016/j.marpetgeo.2014.03.012>
- Menant A, Angiboust S, Gerya T (2019) Stress-driven fluid flow controls long-term megathrust strength and deep accretionary dynamics. *Sci Rep* 9(1):9714
- Obana K, Fujie G, Takahashi T, Yamamoto Y, Nakamura Y, Kodaira S, Takahashi N, Kaneda Y, Shinohara M (2012) Normal-faulting earthquakes beneath the outer slope of the Japan Trench after the 2011 Tohoku earthquake: implications for the stress regime in the incoming Pacific plate. *Geophys Res Lett* 39:1–7
- Peacock SM (1990) Fluid processes in subduction zones. *Science* 248:329–337
- Reston T, Krawczyk C, Klaeschen D (1996) The S reflector west of Galicia (Spain): evidence from prestack depth migration for detachment faulting during continental breakup. *J Geophys Res Solid Earth* 101(B4):8075–8091
- Saffer DM, Silver EA, Fisher AT, Tobin H, Moran K (2000) Inferred pore pressures at the Costa Rica subduction zone: implications for dewatering processes. *Earth Planet Sci Lett* 177(3):193–207. [https://doi.org/10.1016/S0012-821X\(00\)00048-0](https://doi.org/10.1016/S0012-821X(00)00048-0)
- Schlaphorst D, Kendall JM, Collier JS, Verdon JP, Blundy J, Baptie B, Latchman JL, Massin F, Bouin MP (2016) Water, oceanic fracture zones and the lubrication of subducting plate boundaries—insights from seismicity. *Geophys J Int* 204:1405–1420
- Skarbek RM, Saffer DM (2009) Pore pressure development beneath the décollement at the Nankai subduction zone: Implications for plate boundary fault strength and sediment dewatering. *J Geophys Res Solid Earth*. <https://doi.org/10.1029/2008JB006205>
- Somerville P, Irikura K, Graves R, Sawada S, Wald D, Abrahamson N, Iwasaki Y, Kagawa T, Smith N, Kowada A (1999) Characterizing crustal earthquake slip models for the prediction of strong ground motion. *Seismol Res Lett* 70:59–80
- Syracuse EM, van Keken PE, Abers GA (2010) The global range of subduction zone thermal models. *Phys Earth Planet Inter* 183(1–2):73–90
- Taylor B, Hayes DE (1983) Origin and history of the South China Sea basin. *The Tectonic and Geologic Evolution of Southeast Asian Seas and Islands: Part 2*, 90 edited. AGU, Washington, DC, pp 23–56
- Tobin H, Vannucchi P, Meschede M (2001) Structure, inferred mechanical properties, and implications for fluid transport in the décollement zone, Costa Rica Convergent Margin. *Geology* 29(10):907–910. [https://doi.org/10.1130/0091-7613\(2001\)029%3c0907:Simple%3e2.0.Co;2](https://doi.org/10.1130/0091-7613(2001)029%3c0907:Simple%3e2.0.Co;2)
- Tobin H, Henry P, Vannucchi P, Screamor E (2014) Subduction zones: structure and deformation history. *Developments in marine geology*, vol 7. Elsevier, Amsterdam, pp 599–640
- van Keken PE, Hacker BR, Syracuse EM, Abers A (2011) Subduction factory: 4. Depth-dependent flux of H₂O from subducting slabs worldwide. *J Geophys Res Solid Earth*. <https://doi.org/10.1029/2010jb007922>
- Waldhauser F (2001) HypoDD—a program to compute double-difference hypocenter locations. U.S. Geological Survey, United States
- Waldhauser F, Ellsworth WL (2000) A Double-difference Earthquake location algorithm: method and application to the Northern Hayward Fault, California. *Bull Seismol Soc Am* 90:1353–1368
- Wang TK, Chen MK, Lee CS, Xia K (2006) Seismic imaging of the transitional crust across the northeastern margin of the South China Sea. *Tectonophysics* 412(3):237–254. <https://doi.org/10.1016/j.tecto.2005.10.039>
- Wells DL, Coppersmith KJ (1994) New empirical relationships among magnitude, rupture length, rupture width, rupture area, and surface displacement. *Bull Seismol Soc Am* 84:974–1002. <https://doi.org/10.1785/bssa0840040974>
- Worzewski T, Jegen M, Kopp H, Brasse H, Castillo TW (2010) Magnetotelluric image of the fluid cycle in the Costa Rican subduction zone. *Nat Geosci* 4(2):108–111. <https://doi.org/10.1038/ngeo1041>
- Yu SB, Kuo LC, Punongbayan RS, Ramos EG (1999) GPS observation of crustal deformation in the Taiwan-Luzon Region. *Geophys Res Lett* 26(7):923–926. <https://doi.org/10.1029/1999GL900148>
- Zhang F, Lin J, Zhou Z, Yang H, Zhan W (2018a) Intra- and intertrench variations in flexural bending of the Manila, Mariana and global trenches: implications on plate weakening in controlling trench dynamics. *Geophys J Int* 212(2):1429–1449. <https://doi.org/10.1093/gji/ggx488>
- Zhang J, Sun Z, Xu M, Yang H, Zhang Y, Li F (2018b) Lithospheric 3-D flexural modelling of subducted oceanic plate with variable effective elastic thickness along the Manila Trench. *Geophys J Int* 21:2071–2092. <https://doi.org/10.1093/gji/ggy393>

Publisher's Note

Springer Nature remains neutral with regard to jurisdictional claims in published maps and institutional affiliations.

Submit your manuscript to a SpringerOpen® journal and benefit from:

- Convenient online submission
- Rigorous peer review
- Open access: articles freely available online
- High visibility within the field
- Retaining the copyright to your article

Submit your next manuscript at ► [springeropen.com](https://www.springeropen.com)